crystals

MDPI

Article

The Role of Coulomb Interactions for Spin Crossover Behaviors and Crystal Structural Transformation in Novel Anionic Fe(III) Complexes from a π-Extended ONO Ligand

Suguru Murata [1], Kazuyuki Takahashi [1,*], Takahiro Sakurai [2], Hitoshi Ohta [3], Takashi Yamamoto [4], Yasuaki Einaga [4], Yoshihito Shiota [5] and Kazunari Yoshizawa [5]

1 Department of Chemistry, Graduate School of Science, Kobe University, 1-1 Rokkodai, Nada-ku, Kobe, Hyogo 657-8501, Japan; 150s224s@stu.kobe-u.ac.jp
2 Center for Support of Education and Research Activities, Kobe University, 1-1 Rokkodai, Nada-ku, Kobe, Hyogo 657-8501, Japan; tsakurai@kobe-u.ac.jp
3 Molecular Photoscience Research Center, Kobe University, 1-1 Rokkodai, Nada-ku, Kobe, Hyogo 657-8501, Japan; hohta@kobe-u.ac.jp
4 Department of Chemistry, Faculty of Science and Technology, Keio University, 3-14-1 Hiyoshi, Kohoku-ku, Yokohama, Kanagawa 223-8522, Japan; takyama@chem.keio.ac.jp (T.Y.); einaga@chem.keio.ac.jp (Y.E.)
5 Institute for Materials Chemistry and Engineering, Kyushu University, 744 Motooka, Nishi-ku, Fukuoka 819-0395, Japan; shiota@ms.ifoc.kyushu-u.ac.jp (Y.S.); kazunari@ms.ifoc.kyushu-u.ac.jp (K.Y.)
* Correspondence: ktaka@crystal.kobe-u.ac.jp; Tel./Fax: +81-78-803-5691

Academic Editor: Martin T. Lemaire
Received: 30 March 2016; Accepted: 28 April 2016; Published: 3 May 2016

Abstract: To investigate the π-extension effect on an unusual negative-charged spin crossover (SCO) Fe^{III} complex with a weak N_2O_4 first coordination sphere, we designed and synthesized a series of anionic Fe^{III} complexes from a π-extended naphthalene derivative ligand. Acetonitrile-solvate tetramethylammonium (TMA) salt **1** exhibited an SCO conversion, while acetone-solvate TMA salt **2** was in a high-spin state. The crystal structural analysis for **2** revealed that two-leg ladder-like cation-anion arrays derived from π-stacking interactions between π-ligands of the Fe^{III} complex anion and Coulomb interactions were found and the solvated acetone molecules were in one-dimensional channels between the cation-anion arrays. A desolvation-induced single-crystal-to-single-crystal transformation to desolvate compound **2′** may be driven by Coulomb energy gain. Furthermore, the structural comparison between quasi-polymorphic compounds **1** and **2** revealed that the synergy between Coulomb and π-stacking interactions induces a significant distortion of coordination structure of **2**.

Keywords: spin crossover; Coulomb interaction; π-stacking interaction; crystal structural transformation; mononuclear Fe(III) complex; anionic complex; ONO tridentate ligand

1. Introduction

Spin crossover (SCO) is one of a number of switching phenomena, namely a spin-state equilibrium or transition between high-spin (HS) and low-spin (LS) state found in a transition metal coordination complex. Since SCO can be induced by external stimuli such as temperature, pressure, magnetic field, and light, SCO complexes have aroused growing attention as externally-controllable molecular materials [1,2]. Recently the applications of SCO complexes toward memory, display, and sensing devices as well as the development of multifunctional SCO compounds combining SCO with electronic properties such as electrical conductivity [3–7], magnetic property [8–12], and optical property [13,14] are actively studied.

A typical SCO complex is an octahedral six-coordinate complex whose metal center is a Fe^{II}, Fe^{III}, or Co^{II} ion. Since SCO originates from competition between a spin-pairing and ligand-field splitting energy, the occurrence of SCO strongly depends on the number and kind of coordination donor atoms. Usual donor atom sets for SCO Fe^{II} and Fe^{III} complexes are N_6 and N_4O_2, respectively. This means that the ligand field of an SCO Fe^{III} complex is weaker than that of an SCO Fe^{II} complex. Note that the charge of an SCO complex is generally cationic or neutral and, thus, anionic mononuclear SCO complexes are very rare [15–19].

Recently, we discovered unusual anionic SCO Fe^{III} complexes, $(C^+)[Fe^{III}(azp)_2]$ [C^+ = monovalent cation, H_2azp = (2′-hydroxyphenylazo)-2-hydroxybenzene] [20], whose first coordination sphere comprised a N_2O_4 donor atom set assuming a weak ligand-field for Fe^{III} complexes. The density functional theory (DFT) calculations for the $[Fe^{III}(azp)_2]$ complex suggested that orbital interactions between the Fe^{III} atomic orbital and vicinity of frontier orbitals of an azp ligand may enhance the ligand-field splitting energy. To investigate the perturbation of molecular orbitals of a ligand and the introduction of intermolecular π-stacking interactions between Fe^{III} complex anions, we focused on a π-extended naphthalene-substituted ligand, aznp dianion [H_2aznp = (2′-hydroxyphenylazo)-2-hydroxynaphthalene]. The synthesis and magnetic susceptibility of a series of monovalent quaternary onium salts with the $[Fe^{III}(aznp)_2]$ anion (**1**–**5**, Figure 1) revealed that tetramethylammonium (TMA) salts gave quasi-polymorphic acetonitrile-solvate SCO complex (**1**) and acetone-solvate HS complex (**2**). The X-ray crystal structure and thermal analysis for **2** revealed that it was successful to introduce π-stacking interactions between the Fe^{III} anions and moreover a single-crystal-to-single-crystal (SC-SC) structural transformation from acetone-solvate complex **2** to non-solvate complex (**2′**) was induced by desolvation. The structural comparison between the quasi-polymorphic compounds, HS **1**, LS **1**, **2**, and **2′** indicates that Coulomb interactions do not contribute to the cooperativity of SCO phenomenon, whereas the synergy between Coulomb interactions and intermolecular π-stacking interactions induces the distortion of coordination structures of the SCO complex ion, which results in the HS state for **2** and **2′**. Although the role of Coulomb interaction has hardly been described in the studies of SCO complexes to date, the present study discloses the role of Coulomb interactions for charged SCO complexes. We, herein, report the synthesis, magnetic, and thermal property, and crystal structures of a series of the $[Fe^{III}(aznp)_2]$ complexes.

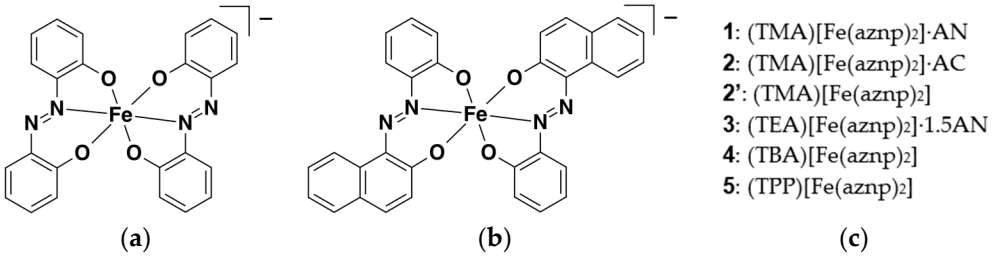

Figure 1. Molecular structures. (**a**) $[Fe^{III}(azp)_2]$ anion; (**b**) $[Fe^{III}(aznp)_2]$ anion; and (**c**) the numberings and formula of compounds **1**–**5**. TMA = tetramethylammonium, TEA = tetraethylammonium, TBA = tetrabutylammonium, TPP = tetraphenylphosphonium, AN = acetonitrile, AC = acetone.

2. Results and Discussion

2.1. Synthesis

2.1.1. Synthesis of Ligand

The H_2aznp molecule and its derivatives were known as azo-dyes. Two different procedures were reported to synthesize H_2aznp. One is one-step azo-coupling reaction of 2-hydroxyphenyl diazonium salt with 2-naphtholate [21] and another is a two-step reaction, namely an azo-coupling reaction using phenyl diazonium salt followed by oxidative hydroxylation of 2-hydroxyphenylazo compound [22].

When we tried to synthesize H_2aznp according to the former procedure, it was not successful to obtain H_2aznp. Since the formation of diazocyclohexadienone is possible [23], the hydroxyl group was protected to prevent 2-hydroxyphenyl diazonium salt from undesired isomerization. According to the synthesis of H_2aznp derivatives [24], the synthesis of H_2aznp was achieved by azo-coupling reaction of 2-methoxyphenyl diazonium salt followed by demethylation using $AlCl_3$ [25] in a moderate yield.

2.1.2. Synthesis of Complexes **1**–**5**

The complexes **1**–**5** were prepared according to the literature procedure [20]. The compositions were confirmed by microanalyses and crystal analyses.

*2.2. Thermogravimetry-Differential Thermal Analysis (TG-DTA) for **1**–**3***

To investigate thermal stability of the solvate compounds **1**–**3**, TG-DTA were performed using a Rigaku TG8120 analyzer. The TG curves are shown in Figure 2. On heating compound **1**, the weight loss was observed at around room temperature. However, consecutive decrease in weight was very gradual and the weight loss reached to 5.9% at 245 °C. Further heating resulted in abrupt decrease in weight, indicative of decomposition of compound **1**. The weight loss ratio at 245 °C exactly corresponded to the weight ratio of one acetonitrile molecule (5.9%). On the other hand, the decrease in weight for **2** started at 75 °C and then the weight loss reached to 8.4% at 145 °C. The weight was almost constant up to 200 °C. The weight loss was in good agreement with the release of one acetone molecule (8.2%) from compound **2**. The difference of the thermal behaviors between **1** and **2** will be discussed in the crystal structure description section. On heating **3**, the weight decreased most rapidly. The weight loss at 120 °C was 8.5%, which was consistent with the loss of 1.5 acetonitrile molecules (8.0%).

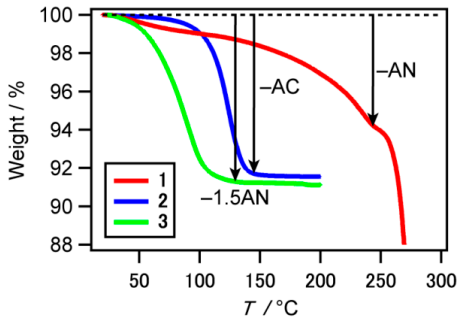

Figure 2. TG curves for compounds **1** (red), **2** (blue), and **3** (green). The scan rate was 2 K· min^{-1}.

After cooling the measured samples, compounds **1** and **3** turned to be a powder and amorphous solid, respectively. The DTA curve suggested that compound **3** melted above 150 °C. Interestingly, we found that compound **2** maintained a crystalline form after the TG measurement. We designate the desolvate crystal as compound **2′** hereafter. To check the possibility of uptake of a small molecule into **2′**, the TG-DTA for the pristine sample **2′** and samples exposed to vapors of common organic solvents revealed no weight loss up to 200 °C. Moreover, the crystalline form **2′** unchanged after the exposure, suggesting that compound **2′** may not have any pore to catch up a small molecule.

*2.3. Magnetic Susceptibility for **1**–**5***

The temperature variations of magnetic susceptibility for compounds **1**–**5** along with the desolvate compound **2′** are shown in Figure 3. The $\chi_M T$ value for acetonitrile-solvate compound **1** at 300 K was 3.75 cm^3 K· mol^{-1}. On cooling the sample, the $\chi_M T$ values were gradually decreased and reached to 1.56 cm^3 K· mol^{-1} at 80 K, suggesting compound **1** exhibited a magnetic transition. This magnetic behavior of **1** was quite similar to that of the parent [$Fe^{III}(azp)_2$] compound [20]. On the other hand,

the $\chi_M T$ values below 80 K were higher than those of the parent compound. There are various possibilities regarding this magnetic transition, namely incomplete SCO conversion between the HS ($S = 5/2$) and LS ($S = 1/2$) state in an Fe^{III} complex, that between the HS ($S = 2$) and LS ($S = 0$) state in an Fe^{II} complex with one semiquinone-like radical ($S = 1/2$), or metal-to-ligand charge transfer (MLCT) transition from an HS Fe^{III} complex ($S = 5/2$) to HS Fe^{II} complex ($S = 2$) antiferromagnetically coupled to a semiquinone-like radical ($S = 1/2$). As discussed in Mössbauer spectroscopy and crystal structures sections, this magnetic transition proves to originate from the SCO conversion in the Fe^{III} complex. The acetone-solvate compound **2** showed a different magnetic behavior. The $\chi_M T$ value for **2** at 300 K was 4.11 cm^3 K· mol^{-1}, indicating that **2** was in the HS state of an Fe^{III} complex. On lowering temperatures, the $\chi_M T$ values were almost constant down to 15 K and then slightly decreased, probably due to zero-field splitting, indicating compound **2** was in the HS state of the Fe^{III} complex in the whole temperature range. Moreover, the magnetic susceptibility of **2′** revealed that desolvation from **2** did not affect the spin-state of the compound. The difference of magnetic behaviors between quasi-polymorphic compounds **1**, **2**, and **2′** is attributed to that of crystal packing effects. The magnetic behaviors for compounds **3**–**5** were less thermally dependent and nearly in the HS state of an Fe^{III} complex. These observations imply that π-extension of ligands for the [Fe(azp)$_2$] compounds favors the HS state.

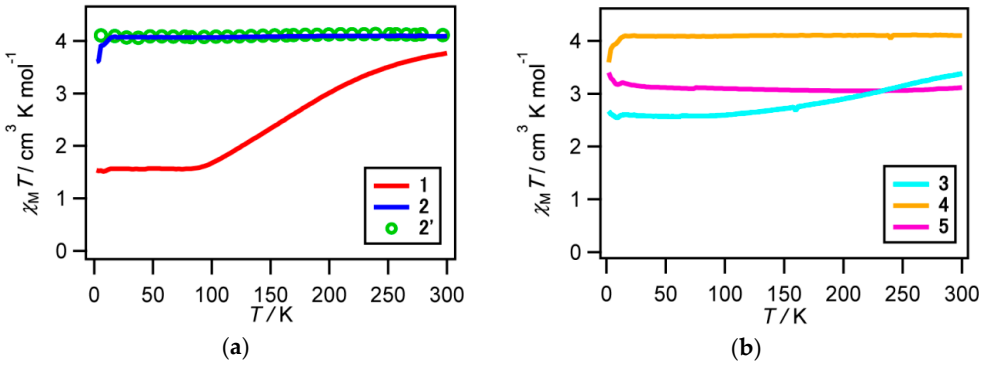

Figure 3. $\chi_M T$ *vs.* T products of the [Fe(aznp)$_2$] compounds. (**a**) acetonitrile-solvate compound **1** (red), acetone-solvate compound **2** (blue), and acetone-desolvate compound **2′** (green circle); (**b**) compounds **3** (cyan), **4** (orange), and **5** (magenta). The scan rate was 2 K· min^{-1}.

2.4. Mössbauer Spectroscopy for ***1***

To confirm the valence and spin states of the Fe ion for compound **1**, the temperature valuable Mössbauer spectra for **1** were recorded at 10.5, 30, 70, 180 and 293 K (Figure 4). The spectrum at 293 K consisted of mainly a broad singlet with a small shoulder, suggesting the overlapping of a doublet spectrum. On lowering temperatures, a quadrupole doublet was developed at 180 K and then the doublet spectra unchanged at 70 K and below. Assuming the observed spectra at 180 and 293 K from a broad singlet and quadrupole doublet, the fitting parameters for isomer shift (IS) and quadrupole splitting (QS) are listed in Table 1. The IS value for a broad singlet is typical of an HS Fe^{III} or LS Fe^{II} complex. If compound **1** consists of LS Fe^{II} center with one semiquinone-like radical, the $\chi_M T$ value of 3.75 cm^3 K· mol^{-1} at 300 K cannot be explained. Therefore, a broad singlet spectrum is ascribed to an HS Fe^{III} complex. The IS value for a quadrupole doublet is typical of an LS Fe^{III} complex. Consequently, the temperature variations in Mössbauer spectra clearly revealed that the magnetic conversion in compound **1** originates from the SCO transition of the Fe^{III} complex. However, it was very difficult to fit the observed spectra from a broad HS singlet and LS quadrupole doublet at 70 K and below. This is probably because an HS singlet is too broad to fit the spectra. The magnetic relaxation due to a weak spin-spin interaction were known to result in broadening or magnetic splitting of a spectrum for magnetically-diluted HS Fe^{III} complexes [26,27]. Therefore, we simulated each observed

spectrum by fixing the isomer shift for HS species at 70 K and below. As compared with the parent [Fe(azp)$_2$] compound [20], the Mössbauer parameters for HS species in **1** are in good agreement of those in the parent compound, while the IS values for LS in **1** are slightly smaller than those in the parent compound.

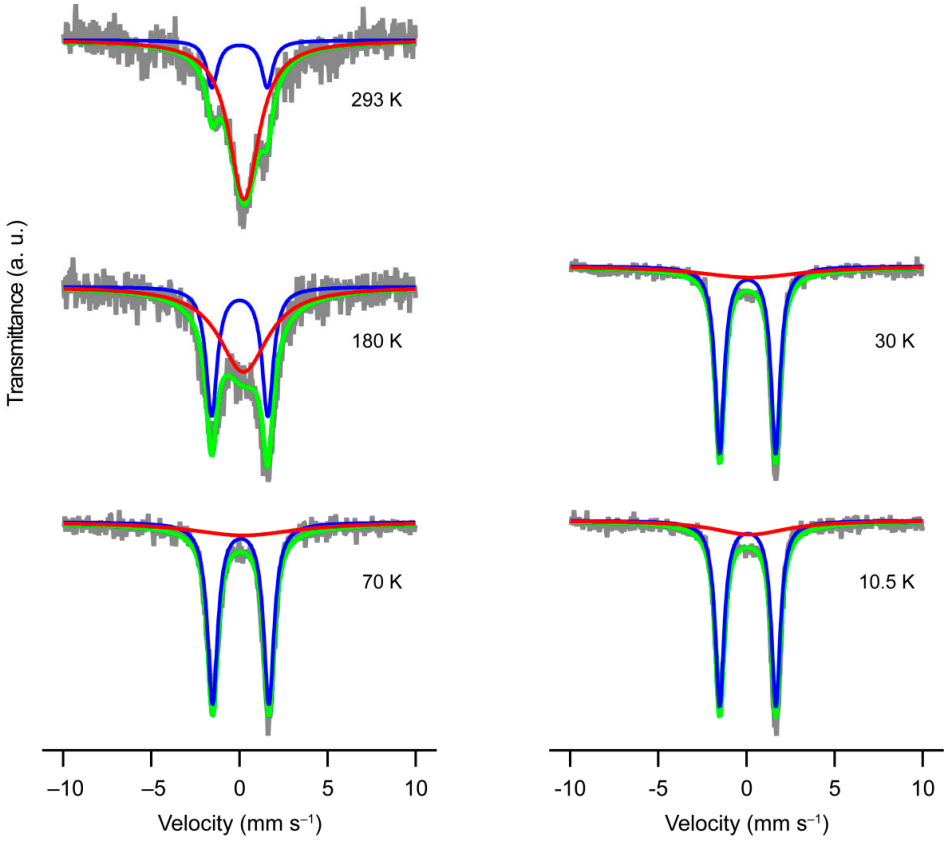

Figure 4. Temperature dependence of Mössbauer spectra for **1**. Gray lines are observed spectra. Red and blue lines indicate the simulated HS and LS spectra, respectively. Green lines are the sum of the simulated HS and LS spectra.

Table 1. Temperature variations of Mössbauer parameters for **1**.

T/K	Spin-State	Ratio	IS [1]/mm· s^{-1}	QS [2]/mm· s^{-1}	LW [3]/mm· s^{-1}
293	HS [4]	82.1%	0.259(17)	–	2.06(11)
	LS [5]	17.9%	0.01(2)	3.13(5)	0.76(11)
180	HS	59.6%	0.22(4)	–	3.4(2)
	LS	40.4%	0.007(9)	3.180(18)	0.76(4)
70	HS	27.8%	0.21(18)	–	7.3(11)
	LS	72.2%	0.07(3)	3.190(6)	0.703(14)
30	HS	26.1%	0.2(6)	–	7.2(9)
	LS	73.9%	0.0640(17)	3.171(4)	0.621(8)
10.5	HS	24.2%	0.2(7)	–	5.1(6)
	LS	75.8%	0.070(2)	3.183(4)	0.609(8)

[1] Isomer shift; [2] Quadrupole splitting; [3] Linewidth; [4] High-spin; [5] Low-spin.

2.5. Crystal Structures of ***1*** *and* ***2***

Single crystal X-ray structural analyses for **1**, **2**, and **2′** were performed using a Bruker AXS APEXII Ultra diffractometer (Bruker AXS, Yokohama, Japan). Fortunately, it was successful to determine the crystal structure of the desolvate compound **2′** despite a poor quality of crystal. Crystallographic data

are listed in Table 2. The crystal structures for **1** at 90 and 273 K were isostructural and belonged to orthorhombic system with *P*bca, whereas the crystal structures of **2** and **2′** belonged to triclinic *P*-1.

Table 2. Crystallographic data for **1** and **2**.

	1		**2**	**2′**
Formula	$C_{38}H_{35}FeN_6O_4$		$C_{39}H_{38}FeN_5O_5$	$C_{36}H_{32}FeN_5O_4$
Formula Weight	695.57		712.59	654.51
Color	black		black	black
Dimension/mm	0.40 × 0.20 × 0.05		0.12 × 0.07 × 0.01	0.10 × 0.10 × 0.02
T/K	90	273	90	296
Crystal system	orthorhombic	orthorhombic	triclinic	triclinic
Space Group	*P*bca	*P*bca	*P*-1	*P*-1
a/Å	18.337(4)	18.323(3)	9.105(4)	9.885(6)
b/Å	16.237(3)	16.463(2)	14.122(6)	12.558(7)
c/Å	22.673(4)	23.132(3)	15.504(6)	14.709(8)
α/°	90	90	64.034(5)	65.497(7)
β/°	90	90	77.865(6)	76.767(7)
γ/°	90	90	81.570(6)	88.750(8)
V/Å^3	6751(2)	6977.8(17)	1748.9(13)	1611.8(15)
Z	8	8	2	2
ρ_{calcd}/gcm^{-3}	1.369	1.324	1.353	1.349
μ (Mo-Kα)	0.497	0.481	0.483	0.515
$2\theta_{max}$/°	54.96	54.96	52.74	38.06
No. Reflections	37753	38952	9261	4190
(R_{int})	(0.0804)	(0.0702)	(0.0245)	(0.0502)
No. Observations	7705	7969	6964	2592
($I > 2.00\sigma(I)$)	(5600)	(5419)	(4929)	(1423)
No. Variables	488	488	457	419
$R1$ ($I > 2.00\sigma(I)$)	0.0878	0.0679	0.0609	0.0821
R (all data)	0.1136	0.0960	0.0972	0.1483
w$R2$ (all data)	0.2246	0.1989	0.1579	0.2391
Residual electron	0.776	0.691	0.768	0.717
density/eÅ^{-3}	−0.755	−0.453	−0.399	−0.284
Goodness of fit	1.062	1.039	1.029	1.051

2.5.1. Molecular Structure Description of the [Fe(aznp)$_2$] Anion in **1**, **2**, and **2′**

All asymmetric units contained one TMA cation and one [Fe(aznp)$_2$] anion and, additionally, one solvent molecule for **1** and **2**. Although a positional disorder of the TMA cation was observed in **1**, there was no orientational disorder of π-ligands in all [Fe(aznp)$_2$] compounds unlike the parent [Fe(azp)$_2$] compounds [20]. The π-ligand molecule was coordinated to a central Fe atom as a tridentate chelate ligand and, thus, two coordinated ligand molecules were arranged in an almost perpendicular manner (Figure 5). Although both azo nitrogen atoms are possible to coordinate to a Fe atom, the nitrogen atom bonding to the phenyl ring was uniquely bound to the Fe atom, resulting in the formation of five-membered and six-membered chelating structures for the phenolate and naphtholate moieties, respectively. This suggests that the steric repulsion between the lone pair of an uncoordinated nitrogen atom and *peri*-hydrogen atom of a naphthalene ring governs the formation of a coordination structure in the [Fe(aznp)$_2$] anion.

The selected coordination bond lengths and distortion parameters are listed in Table 3. As compared with the coordination bond lengths between 90 and 273 K in **1**, the average differences in the Fe–O bond lengths for the six-membered and five-membered chelate side were 0.086(3) and 0.043(3) Å, respectively. On the other hand, the average difference in the Fe–N bond lengths was 0.164(3) Å. The difference of the Fe–O bond lengths was very similar to that of the parent [Fe^{III}(azp)$_2$] compound [20], whereas that of the Fe–N bond lengths was smaller than that of the parent compound. This observation was in good agreement with larger change in the HS/LS ratio in the parent compound. The distortion parameters of Σ, Θ, and ϕ in **1** were largely changed between 90 and 273 K, which corresponded to the HS-LS conversion, whereas the dihedral angles of θ were unchanged. Although there is a possibility

that an MLCT may occur in **1** as described in the magnetic susceptibility section, the differences in the C–O, C–N, and N=N bond lengths between 90 and 273 K were less than 0.01 Å. This observation clearly indicates that the magnetic conversion in **1** originates from the SCO not MLCT transition.

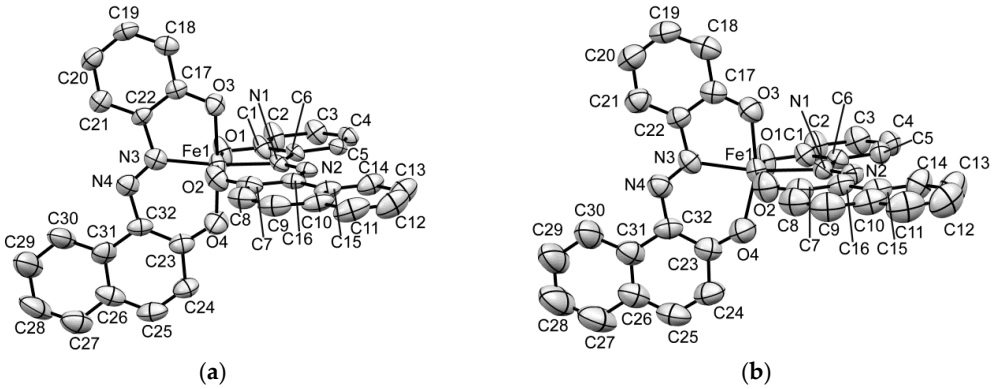

Figure 5. ORTEP drawings of 50% probability with atomic numberings for the [Fe(aznp)$_2$] anion in compound **1**. (**a**) At 90 K; (**b**) At 273 K. Hydrogen atoms are omitted for clarity.

Table 3. Selected coordination bond lengths and distortion parameters for **1**, **2**, and **2′**.

	1	**1**	**2**	**2′**
T/K	90	273	90	296
Fe1-O1/Å	1.913(3)	1.960(2)	1.999(3)	1.983(9)
Fe1-O2/Å	1.878(3)	1.965(3)	1.979(3)	1.959(10)
Fe1-N1/Å	1.952(3)	2.110(2)	2.161(3)	2.146(12)
Fe1-O3/Å	1.936(3)	1.975(3)	1.994(2)	2.009(7)
Fe1-O4/Å	1.884(4)	1.969(3)	1.983(2)	1.998(8)
Fe1-N3/Å	1.967(4)	2.136(3)	2.156(3)	2.130(10)
Σ [1]/°	27.63(15)	80.24(11)	99.67(10)	91.4(4)
Θ [2]/°	46.72(13)	151.24(9)	185.12(9)	172.3(3)
ϕ [3]/°	172.44(15)	168.96(10)	168.30(9)	165.0(4)
θ [4]/°	87.60	87.51	88.97	87.6

[1] The sum of the absolute differences of bite angles from 90°. [2] The sum of the absolute differences of all the angles of triangle surfaces of an coordination octahedron from 60°. [3] The angles of N1-Fe1-N3. [4] Dihedral angles between the mean planes of π-ligands in the [Fe(aznp)$_2$] anion.

Both Fe–O and Fe–N bond lengths of **1** at 273 K were a little shorter than those of **2** at 90 K and **2′** at 296 K, suggesting that the HS fractions of **2** and **2′** were larger than that of **1**. This is consistent with the magnetic susceptibility data. Note that two kinds of distortion parameters of Σ and Θ for **2** and **2′** were much larger than those for **1** at 273 K. This suggests that some crystal packing effects may induce the distortion of a coordination structure.

2.5.2. Crystal Description of **1**

The molecular arrangement for **1** at 273 K is depicted in Figure 6. No notable intermolecular interaction between [Fe(aznp)$_2$] anions and acetonitrile molecules was found in **1**. Short cation$\cdots$anion distances between the nitrogen atoms of the TMA cation and iron atoms of [Fe(aznp)$_2$] anion were 5.549 (a), 5.724 (b), and 5.736 Å (c) at 273 K (Table 4), which formed two-dimensional (2D) honeycomb Coulomb interaction networks parallel to the *ab* plane (Figure 6a). On the other hand, the shortest distance along the *c* axis was 11.760 Å (e) at 273 K. Therefore, the crystal of **1** mainly constructed 2D networks based on Coulomb interactions between cations and anions. At 90 K there was no remarkable difference in the corresponding cation$\cdots$anion distances. This suggests that the Coulomb interactions does not largely affect the SCO behavior.

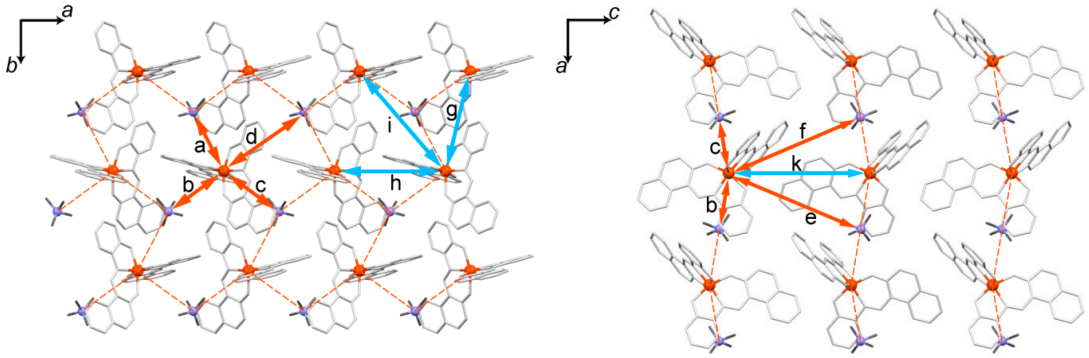

(**a**) (**b**)

Figure 6. Crystal structure of **1** at 273 K. (**a**) Cation-anion arrangement parallel to the *ab* plane; and (**b**) cation-anion arrangement perpendicular to the *ab* plane. Acetonitrile molecules are omitted for clarity. Orange and cyan double arrows indicate neighboring Fe···N and Fe···Fe distances, respectively. Orange dash lines indicate neighboring Fe···N distances shorter than 6 Å. The letters correspond to those in Table 4.

Table 4. The selected intermolecular distances in **1**, **2**, and **2′**.

	1	**1**	**2**	**2′**
T/K	90	273	90	296
Fe···N/Å				
a	5.429(5)	5.549(4)	4.982(3)	5.552(12)
b	5.784(4)	5.724(3)	5.649(4)	5.661(12)
c	5.756(4)	5.736(3)	5.767(4)	5.831(11)
d	8.202(4)	8.275(4)	10.299(5)	10.202(12)
e	11.368(6)	11.810(5)	11.381(5)	9.526(12)
f	11.581(6)	11.760(5)	13.357(5)	11.847(14)
Fe···Fe/Å				
g	8.5622(15)	8.6246(11)	8.183(3)	8.252(5)
h	9.3266(17)	9.2947(13)	8.235(3)	7.925(4)
i	10.7535(16)	10.8840(12)	8.758(3)	9.655(6)
j	–	–	9.105(4)	9.885(6)
k	11.611(2)	11.7504(16)	14.060(5)	13.936(7)
π-distances/Å				
x	–	–	3.44	3.52
y	–	–	–	3.43
z	–	–	–	3.44

The shortest distances between the Fe centers were 8.6246(g) and 8.5622(g) Å at 273 and 90 K, respectively. These values were a little longer than 5.832 Å for $[Fe(pap)_2](ClO_4)\cdot H_2O$ [28] and 7.063 Å for $[Fe(asal)_2](NCSe)CH_2Cl_2$ [29] as similar mononuclear SCO Fe^{III} complexes from π-ligands. These observations might lead to the magnetic relaxation found in Mössbauer spectra in **1**.

2.5.3. Crystal Description of **2**

The molecular arrangement for **2** at 90 K is shown in Figure 7a,c,e. Interestingly, π-stacking interactions between neighboring Fe^{III} complex anions were observed (Figure 7a, green double arrows). The π-plane distance between the naphthyl ring and the centroid of phenyl ring was 3.44 Å (Table 4). The intermolecular π-stacking interactions construct a one-dimensional (1D) Fe anion array along the *a* axis. The short cation···anion distances between the nitrogen atoms of TMA cation and iron atoms of $[Fe(aznp)_2]$ anion along the 1D Fe anion array were 4.982 (a) and 5.649 Å (b) and therefore the TMA cation and $[Fe(aznp)_2]$ anion were alternately arranged along the *a* axis. Moreover, the short cation···anion distances along the *c* axis were calculated to be 5.767 (c) and 10.299 Å (d) between the

1D Fe anion arrays, whereas those along the *b* axis were 11.381 (e) and 13.357 Å (f) (Figure 7c, Table 4). Consequently, two-leg ladder-like cation···anion arrays were formed by π-stacking and Coulomb interactions in compound **2**. Note that solvate acetone molecules existed in the cavity between the two-leg ladder-like arrays and then 1D channels perpendicular to the arrays were found along the *b* axis (Figure 7e). However, the thermal stability of compound **2** observed in the TG measurement is not consistent with this channel structure. One possible reason is that the diameter size of 1D channels are smaller than the molecular size of acetone. Another is electrostatic and hydrogen bonding interactions between acetone molecules and TMA cations, because all acetone molecules were arranged in a manner directing the oxygen atom to the TMA cation and the distance between the nitrogen atom of the cation and the oxygen atom of acetone molecule was 3.785 Å, and the C(TMA cation)···O distances were 3.343 and 3.366 Å.

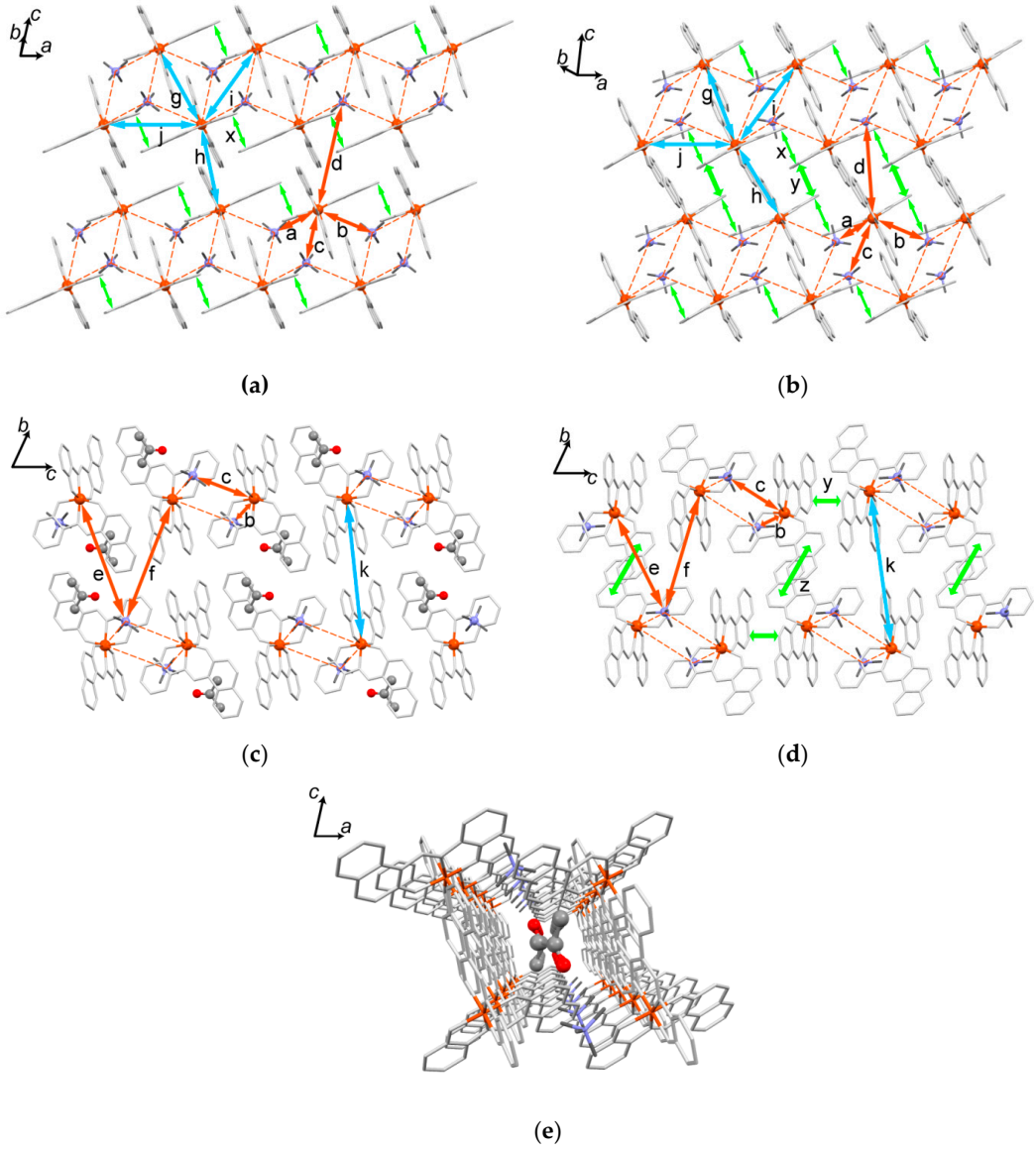

Figure 7. Crystal structures parallel to two-leg ladder-like cation···anion arrays for **2** (**a**) and **2′** (**b**). Acetone molecules are omitted for clarity; Crystal structures perpendicular to the two-leg ladder-like cation···anion arrays for **2** (**c**) and **2′** (**d**); (**e**) 1D channel structure along the *b* axis in **2**. Orange, cyan, and green double arrows indicate neighboring Fe···N, Fe···Fe distances, and π-stacking interactions, respectively. Orange dash lines indicate Fe···N distances shorter than 6 Å. The letters correspond to those in Table 4.

2.5.4. Desolvation-Induced Crystal Structure Transformation from **2** to **2′**

The molecular arrangement for **2′** at 293 K is shown in Figure 7b,d. The TG measurement and single crystal structural analysis for **2′** revealed that an SC-SC structural transformation from **2** to **2′** occurred upon desolvation. The crystal system and space group were unchanged accompanying the SC-SC transformation. The SC-SC transformation resulted in the shortening of 1.6 Å along the *b* axis and 0.8 Å along the *c* axis, whereas the lengthening of 0.8 Å along the *a* axis. These changes in the cell parameters were rationalized by the motion to fill in the cavities given by the release of acetone molecules as compared between Figure 7c,d. The crystal structure of **2′** maintained the two-leg ladder-like molecular arrays in **2**. The short cation$\cdots$anion distances in the two-leg ladder-like arrays (a, b, c) were slightly changed, whereas those between them (e, f) were significantly shortened. Note that π-stacking interactions between the neighboring two-leg ladder-like molecular arrays appeared along both the *b* and *c* axis (Figure 7d, Table 4). Consequently, 2D π-stacking interaction networks parallel to the *ac* plane in **2′** were connected by the Coulomb interactions, affording 3D closed-packing structure. Since the Coulomb interaction and π-stacking interaction are long-distance and short-distance interactions, respectively, the SC-SC transformation may be driven by the Coulomb energy gains due to the shrinkage of cation$\cdots$anion distances.

2.5.5. Structural Comparison between **1**, **2**, and **2′**

As compared with the crystal structures of **1** and **2**, the crystal of **1** comprised 2D honeycomb Coulomb interaction networks, whereas that of **2** consisted of two-leg ladder-like arrays based on Coulomb and π-stacking interactions. Very interestingly, the nearer cation$\cdots$anion distances for compounds **1** and **2** were found to be almost similar in a range of 4.9–5.8 Å with a coordination number of 3, and moreover those between the interaction networks were also similar in a range of 11–13 Å (Table 4). Furthermore, the short cation$\cdots$anion distances for the parent compound are 5.426, 5.777, and 5.812 Å [20]. These observations imply that Coulomb interactions contribute to similar magnitude of lattice energies for the quasi-polymorphic compounds **1** and **2** as well as the parent compound. The difference in the crystal structures for **1** and **2** arises from the competition between π-stacking interactions and crystal packing effects including different solvate molecules. Note that a considerable distortion of the coordination structure of [Fe(aznp)$_2$] anion was found in **2**, whereas the two-leg ladder-like arrays remained after undergoing the SC-SC transformation from **2** to **2′**. These indicate that Coulomb interactions as well as π-stacking interactions play a key role in the formation of two-leg ladder-like arrays in **2** and **2′**. On the other hand, only the similar magnitude of Coulomb interactions observed in **1** and the parent compound resulted in no significant distortion of the coordination structure and, moreover, do not contribute to the cooperativity of SCO. Therefore, the synergistic energy gains from Coulomb interactions and π-stacking interactions may lead to a considerable distortion of the coordination structure of [Fe(aznp)$_2$] anion, leading to the HS state for compounds **2** and **2′**.

2.6. Density Functional Theory (DFT) Calculations

To provide an insight into the π-extension effect on a ligand field splitting energy, the DFT calculations were carried out by using the hybrid B3LYP functional with the Wachters-Hay basis set for Fe and the 6-31 + G(d) basis set for C, H, N, and O. The atomic coordinates for the HS and LS states of an [Fe(aznp)$_2$] anion were taken from the single crystal structural data of **1**. The optimized coordination structures for the [Fe(aznp)$_2$] anions were in good agreement with the corresponding crystal structures for **1**. The energy level diagrams of the occupied α-spin molecular orbitals (MOs) and the selected MO surfaces for the HS [Fe(aznp)$_2$] anion along with those of the HS [Fe(azp)$_2$] anion [20] are depicted in Figure 8. The Fe e_g-like orbitals were contributed to the 150th and 147th MOs for the HS [Fe(aznp)$_2$] anion, which corresponded to the 123th and 121st MOs for the HS [Fe(azp)$_2$] anion, respectively. The Fe t_{2g}-like orbitals were observed in the 135th and 134th MOs for the HS [Fe(aznp)$_2$]

anion, and the 109th and 111th MOs for the HS [Fe(azp)$_2$] anion. Compared with the energy levels of the corresponding MOs between the [Fe(aznp)$_2$] and [Fe(azp)$_2$] anion, the π-extension of a ligand leads to slight stabilization of the MOs containing Fe *d* orbitals except the 135th MO containing π-orbital contribution from the naphtholate moiety. The stabilization of the MOs can be explained by similarly lowering the energies of an anionic π-ligand orbital by π-extension. On the other hand, the increase in 135th orbital energy suggests that the orbital interactions between Fe e_g-like orbital and O π-orbital of the naphtholate moiety may be enhanced by π-extension. Although this leads to slight decrease in the ligand-field splitting energy of the [Fe(aznp)$_2$] anion, a series of the [Fe(aznp)$_2$] complexes were still in the SCO region but their HS fractions were relatively increased as shown in the magnetic susceptibility section.

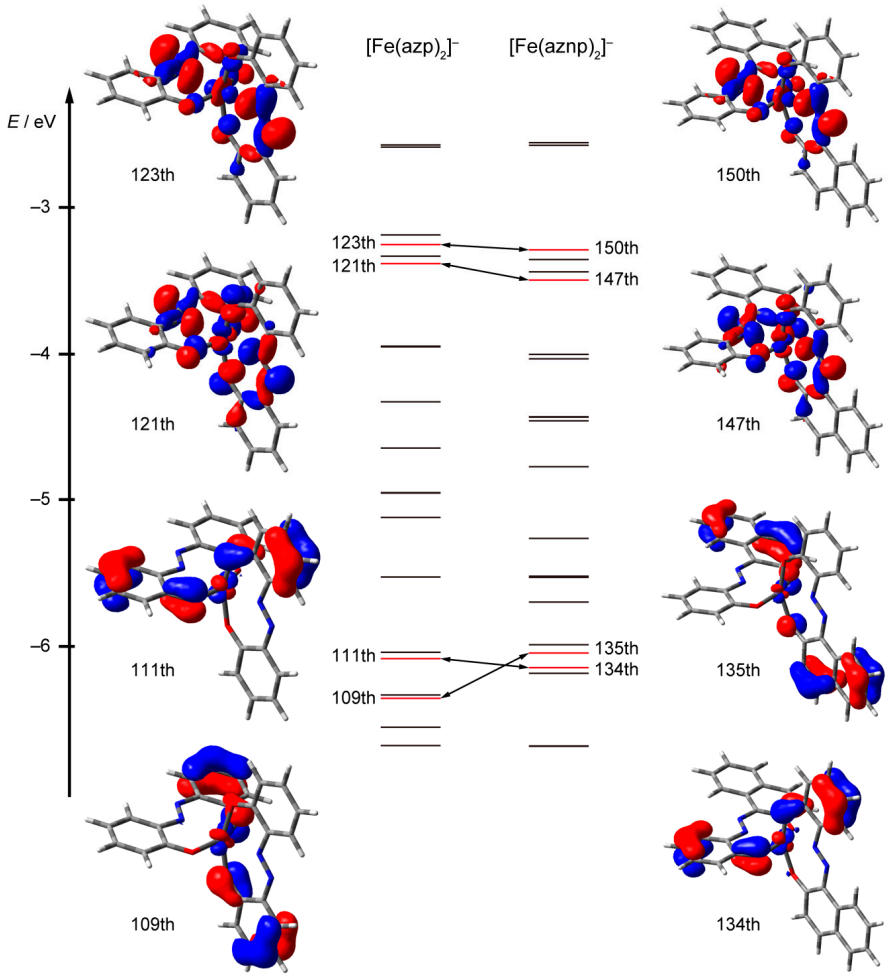

Figure 8. Energy level diagram of the frontier occupied α-spin MOs for HS [Fe(azp)$_2$] and HS [Fe(aznp)$_2$] anions. Red energy levels indicate the MOs containing Fe d-orbital contributions and these surfaces are shown. Double-head arrows indicate the corresponding MOs between HS [Fe(azp)$_2$] and HS [Fe(aznp)$_2$] anions.

3. Materials and Methods

3.1. Synthesis

3.1.1. Synthesis of (2′-methoxyphenylazo)-2-hydroxynaphthalene (MeHaznp)

A solution of 2-methoxyaniline (1.09 g, 8.87 mmol) in 12.3 mL of 2.2 M HCl solution was stirred and cooled to 3 °C. To the dark red solution was added dropwise a solution of $NaNO_2$ (0.67 g,

9.76 mmol) in 1.2 mL of water. The mixture solution turned to be yellowish brown and kept below 5 °C. After confirming the existence of HNO_2 using a KI-starch paper, the solution was quickly transferred to a suspension of β-naphthol (1.28 g, 8.87 mmol) in 15 mL of a aqueous solution of NaOH (0.58 g, 14.5 mmol). The resulting suspension was stirred for 30 min below 5 °C and then warned to room temperature. To this suspension was added 2 mL of 3.5% HCl and stirred. The precipitate was filtered and dried *in vacuo*. Recrystallization from ethyl acetate gave as red needles (1.76 g, 71%). m.p. 184–185 °C. ^{1}H NMR (400 MHz, $CDCl_3$) δ 8.51 (d. *J* = 8.1 Hz, 1H), 8.06 (dd, *J* = 1.5 Hz, 8.0 Hz, 1H), 7.66 (d. *J* = 9.5 Hz, 1H), 7.50–7.55 (m, 2H), 7.36 (ddd, *J* = 1.2 Hz, 7.5 Hz, 14.9 Hz, 1H), 7.20–7.24 (m, 1H), 7.09 (t, *J* = 7.5 Hz, 1H), 7.00 (dd, *J* = 0.9 Hz, 8.2 Hz, 1H), 6.80 (d, *J* = 9.6 Hz, 1H), 4.03 (s, 3H) ppm. ^{13}C NMR (100 MHz, $CDCl_3$) δ 176.97, 149.74, 140.85, 133.80, 132.32, 130.77, 128.93, 128.67, 127.91, 126.97, 126.47, 125.85, 121.71, 121.57, 115.97, 111.24, 56.00 ppm. ESI-MS (*m*/*z*) Calcd for $C_{17}H_{14}N_2O_2$: 278.31. Found: 279.6 (M + H^+), 280.6 (M + $2H^+$). Anal. Calcd. for $C_{17}H_{14}N_2O_2$: C, 73.37; H, 5.07; N, 10.07%. Found: C, 73.21; H, 5.12; N, 9.89%.

3.1.2. Synthesis of H_2aznp

To a stirred solution of MeHaznp (2.00 g, 7.19 mmol) in 144 mL of chloroform was added portionwise a finely powdered $AlCl_3$ (5.75 g, 43.1 mmol). The resulting red suspension was warmed to 30 °C and then 15 mL of pyridine was added dropwise to this suspension. The mixture was heated to reflux for 1.5 h and then cooled to room temperature. The mixture was poured into 150 mL of ice water and then acidified by adding 30 mL of 36% HCl. After evaporating chloroform, the mixture was heated at 80 °C overnight. The resulting pale violet suspension was filtered and brown precipitate was dried *in vacuo*. Recrystallization from ethyl acetate gave **L** as green platelets (1.31 g, 69%). m.p. 196–197 °C (192 °C [21]). ^{1}H NMR (400 MHz, $CDCl_3$) δ 14.52 (s, 1H), 12.42 (s, 1H), 8.25 (d, *J* = 8.4 Hz, 1H), 7.85 (d. *J* = 9.1 Hz, 1H), 7.80 (d, *J* = 8.0 Hz, 1H), 7.71 (dd, *J* = 1.6 Hz, 7.9 Hz, 1H), 7.64 (ddd, *J* = 1.3 Hz, 7.0 Hz, 8.4 Hz, 1H), 7.47 (ddd, *J* = 1.1 Hz, 7.0 Hz, 8.0 Hz, 1H), 7.35 (ddd, *J* = 1.6 Hz, 7.3 Hz, 8.6 Hz, 1H), 7.19 (d, *J* = 9.1 Hz, 1H), 7.06–7.12 (m, 2H) ppm. ^{13}C NMR (100 MHz, $CDCl_3$) δ 155.84, 152.53, 135.92, 134.45, 132.20, 131.14, 129.45, 128.87, 128.84, 128.46, 127.91, 124.98, 120.51, 120.41, 120.35, 118.52 ppm. ESI-MS (*m*/*z*) Calcd for $C_{16}H_{12}N_2O_2$: 264.28. Found: 265.6 (M+H^+). Anal. Calcd. for $C_{16}H_{12}N_2O_2$: C, 72.72; H, 4.58; N, 10.60%. Found: C, 72.58; H, 4.58; N, 10.48%.

3.1.3. General Synthetic Procedure of the [Fe(aznp)$_2$] Compounds (**1**–**5**)

To a red solution of H_2aznp (500 mg, 1.89 mmol) in 15 mL of methanol was added dropwise a methanol solution of sodium methoxide (4.16 mmol) at 60 °C. The solution turned to be dark violet. After stirring for 1.5 h, to this solution was added a solution of $FeCl_3$ (156 mg, 0.96 mmol) in 9 mL of methanol and then stirred for 1 h. To the solution was added corresponding quaternary bromide salts (2.37 mmol) in 15 mL of methanol. After evaporating, the residue was washed by water and dried *in vacuo.* (TMA)[Fe(aznp)$_2$]·AN (**1**): 793 mg of crude TMA salt was obtained. Recrystallization of 100 mg of the crude salt from acetonitrile-diethyl ether gave 71 mg of **1** as black platelets. Anal. Calcd. For $C_{38}H_{35}FeN_6O_4$: C, 65.62; H, 5.07; N, 12.08%. Found: C, 65.54; H, 5.16; N, 11.84%. (TMA)[Fe(aznp)$_2$]·AC (**2**): Recrystallization of 50 mg of the crude TMA salt from acetone-diethyl ether gave 34.3 mg of **2** as black platelets. Anal. Calcd. For $C_{39}H_{38}FeN_5O_5$: C, 65.73; H, 5.38; N, 9.83%. Found: C, 65.92; H, 5.45; N, 9.83%. (TEA)[Fe(aznp)$_2$]·1.5AN (**3**): 880 mg of crude TEA salt was obtained. Recrystallization of 30 mg of the crude TEA salt from acetonitrile-diethyl ether gave 20.8 mg of **3** as black platelets. Anal. Calcd. for $C_{43}H_{44.5}FeN_{6.5}O_4$: C, 66.88; H, 5.81; N, 11.79%. Found: C, 66.61; H, 5.93; N, 11.77%. (TBA)[Fe(aznp)$_2$] (**4**): 950 mg of crude TBA salt was obtained. Recrystallization of 50 mg of the crude TBA salt from acetone-diethyl ether gave 26.1 mg of **4** as black blocks. Anal. Calcd. for $C_{48}H_{56}FeN_5O_4$: C, 70.06; H, 6.86; N, 8.51%. Found: C, 69.86; H, 7.10; N, 8.22%. (TPP)[Fe(aznp)$_2$] (**5**): 871 mg of crude TPP salt was obtained. Recrystallization of 50 mg of the crude TPP salt from acetone-diethyl ether gave 33.3 mg of **5** as black needles. Anal. Calcd. for $C_{56}H_{40}FeN_4O_4P$: C, 73.13; H, 4.38; N, 6.09%. Found: C, 73.11; H, 4.56; N, 5.97%.

3.2. Physical Measurements

Variable temperature direct current magnetic susceptibilities of polycrystalline samples (*ca.* 20 mg) fold in an aluminum foil were measured on a Quantum Design MPMS-XL magnetometer under a field of 0.5 T at a sweep speed of 2 K· min^{-1} in the temperature range of 2–300 K. The sample magnetization data were obtained by the subtraction of background magnetization data for an aluminum foil from the measured data, and then the magnetic susceptibilities were corrected for diamagnetic contributions estimated by Pascal constants [30].

The Mössbauer spectra were recorded on a constant acceleration spectrometer with a source of ^{57}Co/Rh in the transmission mode. The measurements at low temperature were performed with a closed-cycle helium refrigerator (Iwatani Co., Ltd. Tokyo, Japan). Velocity was calibrated by using an α-Fe standard. The obtained Mössbauer spectra were fitted with symmetric Lorentzian doublets by the least squares fitting program (MossWinn).

3.3. Crystal Structure Determinations

A needle crystal was mounted in a polyimide loop. A nitrogen gas flow temperature controller was used for the temperature variable measurements. All data were collected on a Bruker APEX II CCD area detector with monochromated Mo-$K\alpha$ radiation generated by a Bruker Turbo X-ray Source coupled with a Helios multilayer optics. All data collections and calculations were performed using the APEX2 crystallographic software package (Bruker AXS). The data were collected to a maximum 2θ value of 55.0°. A total of 720 oscillation images were collected. The APEX II program was used to determine the unit cell parameters and for data collection. Data were integrated by using SAINT. Numerical absorption correction was applied by using SADABS. The structures at all temperatures were solved by direct methods and refined by full-matrix least-squares methods based on F^2 by using the SHELXTL program. All non-hydrogen atoms were refined anisotropically. Hydrogen atoms were generated by calculation and refined using the riding model. CCDC 1471055-1471058 (**1**, **2**, **2′**) contains the supplementary crystallographic data for this paper. These data can be obtained free of charge via http://www.ccdc.cam.ac.uk/conts/retrieving.html (or from the CCDC, 12 Union Road, Cambridge CB2 1EZ, UK; Fax: +44 1223 336033; E-mail: deposit@ccdc.cam.ac.uk). Preliminary crystal analysis data for **3**, **4**· C_6H_5Cl, and **5** includes the CIFs in the supporting information.

3.4. DFT Calculations

All theoretical calculations were performed using the Gaussian 09 program package [31]. All calculations of the compounds were carried out at the B3LYP functional [32,33]. The Wachters-Hay basis set [34,35] for Fe atoms and the 6-31 + G(d) basis set [36] for H, C, O, and N atoms were used. No imaginary frequencies were found in the optimized structures. Cartesian coordinates of HS [Fe(aznp)$_2$] and LS [Fe(aznp)$_2$] anions calculated by the B3LYP level of theory are summarized in Tables S1 and S2.

4. Conclusions

We report here the synthesis, crystal structures, thermal and magnetic properties of a series of the [Fe(aznp)$_2$] compounds to investigate the π-extension effect on the novel negative-charged SCO [Fe^{III}(azp)$_2$] complex. Since the occurrence of the SCO transition in the acetonitrile-solvate TMA salt was evidenced by the temperature variations in magnetic susceptibility, Mössbauer spectrum, and crystal structure, the SCO phenomenon found in the parent [Fe(azp)$_2$] compound was not specific, and the N_2O_4 coordination sphere for the Fe^{III} ion can provide a ligand-field splitting energy in the SCO region. The DFT calculations suggested the π-extension effect reduced the ligand-field splitting energy. Further investigations on either substitutions on the azp ligand or ligand substitutions to ligands having different kinds of N and/or O donor atoms from the phenolate and azo group are needed to clarify the SCO conditions for the $Fe^{III}N_2O_4$ coordination sphere.

Furthermore, the comparison between the crystal structures for quasi-polymorphic compounds **1** and **2** indicated that only coulombic interactions do not contribute to the cooperativity of SCO phenomenon, whereas the desolvation-induced SC-SC transformation from **2** to **2′** revealed that coulombic interactions play a key role in the lattice energies for the SCO complexes composed of cation and anion components and the molecular distortion of an SCO complex ion resulting from the coexistence with directional intermolecular π-stacking interactions. Since the enhancement of non-covalent intermolecular interactions by coulombic interactions was recently reported in the multifunctional SCO compound [12], taking into account of the charges of metal complex components as well as introduction of intermolecular interactions will be important to design charged multifunctional SCO complexes.

Supplementary Materials: The following are available online at http://www.mdpi.com/2073-4352/6/5/49/s1, Table S1: Cartesian coordinates of the HS [Fe(aznp)$_2$] anion, Table S2: Cartesian coordinates of the LS [Fe(aznp)$_2$] anion, 3.cif: Crystal analysis data for compound **3**, 4_CB.cif: Preliminary crystal analysis data for compound **4**·C_6H_5Cl, 5.cif: Preliminary crystal analysis data for compound **5**.

Acknowledgments: This work was partially supported by JSPS KAKENHI Grant Number 25410068.

Author Contributions: Kazuyuki Takahashi conceived and designed the experiments; Suguru Murata performed the experiments; Suguru Murata and Kazuyuki Takahashi analyzed the data; Takahiro Sakurai and Hitoshi Ohta contributed magnetic susceptibility measurements; Takashi Yamamoto and Yasuaki Einaga contributed Mössbauer spectroscopy; Yoshihito Shiota and Kazunari Yoshizawa contributed theoretical calculations; Kazuyuki Takahashi wrote the paper.

Conflicts of Interest: The authors declare no conflict of interest.

References

1. Gütlich, P.; Goodwin, H.A. Spin crossover—An overall perspective. In *Spin Crossover in Transition Metal Compounds*; Gütlich, P., Goodwin, H.A., Eds.; Springer-Verlag: Berlin, Heidelberg, Germany, 2004; Volume 1, pp. 1–47.
2. Halcrow, M.A., Ed.; *Spin-Crossover Materials*; John Wiley & Sons, Ltd.: Oxford, UK, 2013.
3. Takahashi, K.; Cui, H.-B.; Okano, Y.; Kobayashi, H.; Einaga, Y.; Sato, O. Electrical conductivity modulation coupled to a high-spin—Low-spin conversion in the molecular system [Fe^{III}(qsal)$_2$][Ni(dmit)$_2$]$_3$· CH_3CN· H_2O. *Inorg. Chem.* **2006**, *45*, 5739–5741. [CrossRef] [PubMed]
4. Takahashi, K.; Cui, H.-B.; Okano, Y.; Kobayashi, H.; Mori, H.; Tajima, H.; Einaga, Y.; Sato, O. Evidence of the chemical uniaxial strain effect on electrical conductivity in the spin-crossover conducting molecular system: [Fe^{III}(qnal)$_2$][Pd(dmit)$_2$]$_5$· acetone. *J. Am. Chem. Soc.* **2008**, *130*, 6688–6689. [CrossRef] [PubMed]
5. Djukic, B.; Lemaire, M.T. Hybrid Spin-crossover conductor exhibiting unusual variable-temperature electrical conductivity. *Inorg. Chem.* **2009**, *48*, 10489–10491. [CrossRef] [PubMed]
6. Nihei, M.; Takahashi, N.; Nishikawa, H.; Oshio, H. Spin-crossover behavior and electrical conduction property in iron(II) complexes with tetrathiafulvalene moieties. *Dalton Trans.* **2011**, *40*, 2154–2156. [CrossRef] [PubMed]
7. Phan, H.; Benjamin, S.M.; Steven, E.; Brooks, J.S.; Shatruk, M. Photomagnetic response in highly conductive iron(II) spin- crossover complexes with TCNQ radicals. *Angew. Chem. Int. Ed.* **2015**, *54*, 823–827.
8. Nihei, M.; Tahira, H.; Takahashi, N.; Otake, Y.; Yamamura, Y.; Saito, K.; Oshio, H. Multiple bistability and tristability with dual spin-state conversions in [Fe(dpp)$_2$][Ni(mnt)$_2$]$_2$· $MeNO_2$. *J. Am. Chem. Soc.* **2010**, *132*, 3553–3560. [CrossRef] [PubMed]
9. Ohkoshi, S.; Imoto, K.; Tsunobuchi, Y.; Takano, S.; Tokoro, H. Light-induced spin-crossover magnet. *Nat. Chem.* **2011**, *3*, 564–569. [CrossRef] [PubMed]
10. Ababei, R.; Pichon, C.; Roubeau, O.; Li, Y.-G.; Bréfuel, N.; Buisson, L.; Guionneau, P.; Mathonière, C.; Clérac, R. Rational design of a photomagnetic chain: Bridging single-molecule magnets with a spin-crossover complex. *J. Am. Chem. Soc.* **2013**, *135*, 14840–14853. [CrossRef] [PubMed]
11. Fukuroi, K.; Takahashi, K.; Mochida, T.; Sakurai, T.; Ohta, H.; Yamamoto, T.; Einaga, Y.; Mori, H. Synergistic spin transition between spin crossover and spin-Peierls-like singlet formation in the halogen-bonded molecular hybrid system: [Fe(Iqsal)$_2$][Ni(dmit)$_2$]· CH_3CN· H_2O. *Angew. Chem. Int. Ed.* **2014**, *53*, 1983–1986. [CrossRef] [PubMed]

12. Okai, M.; Takahashi, K.; Sakurai, T.; Ohta, H.; Yamamoto, T.; Einaga, Y. Novel Fe(II) spin crossover complexes involving a chalcogen-bond and π-stacking interactions with a paramagnetic and nonmagnetic $M(dmit)_2$ anion (M = Ni, Au; dmit = 4,5-dithiolato-1,3-dithiole-2-thione). *J. Mater. Chem. C* **2015**, *3*, 7858–7864. [CrossRef]
13. Ohkoshi, S.; Takano, S.; Imoto, K.; Yoshikiyo, M.; Namai, A.; Tokoro, H. 90-degree optical switching of output second-harmonic light in chiral photomagnet. *Nat. Photonics* **2014**, *8*, 65–71. [CrossRef]
14. Wang, C.F.; Li, R.-F.; Chen, X.-Y.; Wei, R.-J.; Zheng, L.-S.; Tao, J. Synergetic spin crossover and fluorescence in one-dimensional hybrid complexes. *Angew. Chem. Int. Ed.* **2015**, *54*, 1574–1577. [CrossRef] [PubMed]
15. Zelentsov, V.V. Spin transitions in iron(III) complexes with thiosemicarbazones of *O*-hydroxyaldehydes. *Sov. Sci. Rev. B Chem.* **1987**, *10*, 485–512.
16. Floquet, S.; Boillot, M.-L.; Rivière, E.; Varret, F.; Boukheddaden, K.; Morineau, D.; Négrier, P. Spin transition with a large thermal hysteresis near room temperature in a water solvate of an iron(III) thiosemicarbazone complex. *New J. Chem.* **2003**, *27*, 341–348. [CrossRef]
17. Floquet, S.; Guillou, N.; Négrier, P.; Rivière, E.; Boillot, M.-L. The crystallographic phase transition for a ferric thiosemicarbazone spin crossover complex studied by X-ray powder diffraction. *New J. Chem.* **2006**, *30*, 1621–1627. [CrossRef]
18. Cook, C.; Habib, F.; Aharen, T.; Clérac, R.; Hu, A.; Murugesu, M. High-temperature spin crossover behavior in a nitrogen-rich Fe^{III}-based system. *Inorg. Chem.* **2013**, *52*, 1825–1831. [CrossRef] [PubMed]
19. Hirosawa, N.; Oso, Y.; Ishida, T. Spin crossover and light-induced excited spin-state trapping observed for an iron(II) complex chelated with tripodal tetrakis(2-pyridyl)methane. *Chem. Lett.* **2012**, *41*, 716–718. [CrossRef]
20. Takahashi, K.; Kawamukai, K.; Okai, M.; Mochida, T.; Sakurai, T.; Ohta, H.; Yamamoto, T.; Einaga, Y.; Shiota, Y.; Yoshizawa, K. A new family of anionic Fe^{III} spin crossover complexes featuring a weak-field N_2O_4 coordination octahedron. *Chem. Eur. J.* **2016**, *22*, 1253–1257. [CrossRef] [PubMed]
21. Drew, H.D.K.; Landquist, J.K. Structure of the cooper lakes of azo-dyes. *J. Chem. Soc.* **1938**, 292–304. [CrossRef]
22. Mitra, S.; Biswas, H.; Bandyopadhyay, P. Synthesis, spectral properties and redox behaviour of *cis*-dioxo-molybdenum(IV) complexes with tridentate arylazo ligands. *Polyhedron* **1995**, *14*, 1581–1584. [CrossRef]
23. Schweig, A.; Baumgartl, H.; Schulz, R. IR and UV matrix photochemistry and solvent effects: The isomerization of diazocyclohexadienones (ortho quinone diazides)—Detection of molecules with the 1,2,3-benzoxadiazole structure. A UV/Vis and IR absorption and UV photoelectron spectroscopic investigation. *J. Mol. Struct.* **1991**, *247*, 135–171.
24. Schetty, G. Neuartige Isomeriefälle bei 1:2-Cr^{III}- und Co^{III}-Komplexen von *o*,*o*'-Dihydroxyazoverbindungen: Pyramidal gebundener Stickstoff mit hoher Inversionsbarriere? *Helv. Chim. Acta* **1970**, *53*, 1437–1459. [CrossRef]
25. Haghbeen, K.; Tan, E.W. Facile synthesis of catechol azo dyes. *J. Org. Chem.* **1998**, *63*, 4503–4505. [CrossRef]
26. Wignall, J.W.G. Mössbauer line broadening in trivalent iron compounds. *J. Chem. Phys.* **1966**, *44*, 2462–2467. [CrossRef]
27. Sano, H. On the spin relaxation of ^{57}Fe(III) species produced through EC-decay in diamagnetic ^{57}Co-labelled Co(III) compounds. *J. Radioanal. Chem.* **1977**, *36*, 105–111. [CrossRef]
28. Hayami, S.; Gu, Z.; Shiro, M.; Einaga, Y.; Fujishima, A.; Sato, O. First observation of light-induced excited spin state trapping for an Iron(III) complex. *J. Am. Chem. Soc.* **2000**, *122*, 7126–7127. [CrossRef]
29. Hayami, S.; Gu, Z.; Yoshiki, H.; Fujishima, A.; Sato, O. Iron(III) spin-crossover compounds with a wide apparent thermal hysteresis around room temperature. *J. Am. Chem. Soc.* **2001**, *123*, 11644–11650. [CrossRef] [PubMed]
30. König, E. *Landolt-Börnstein Neue Serie Gruppe II*; Hellwege, K.-H., Hellwege, A.M., Eds.; Springer-Verlag: Berlin, Heidelberg, Germany; New York, NY, USA, 1966; Volume 2, pp. 1-16–1-18.
31. Frisch, M.J.; Trucks, G.W.; Schlegel, H.B.; Scuseria, G.E.; Robb, M.A.; Cheeseman, J.R.; Scalmani, G.; Barone, V.; Mennucci, B.; *et al. Gaussian 09*, Revision D.01; Gaussian, Inc.: Wallingford, CT, USA, 2009.
32. Becke, A.D. A new mixing of hartree-fock and local density-functional theories. *J. Chem. Phys.* **1993**, *98*, 1372–1377. [CrossRef]
33. Lee, C.; Yang, W.; Parr, R.G. Development of the colle-salvetti correlation-energy formula into a functional of the electron density. *Phys. Rev. B* **1988**, *37*, 785–789. [CrossRef]

34. Wachters, A.J.H. Gaussian basis set for molecular wavefunctions containing third-row atoms. *J. Chem. Phys.* **1970**, *52*, 1033–1036. [CrossRef]
35. Hay, P.J. Gaussian basis sets for molecular calculations. The representation of 3D orbitals in transition-metal atoms. *J. Chem. Phys.* **1977**, *66*, 4377–4384. [CrossRef]
36. Ditchfield, R.; Hehre, W.J.; Pople, J.A. Self-consistent molecular-orbital methods. IX. An extended gaussian-type basis for molecular-orbital studies of organic molecules. *J. Chem. Phys.* **1971**, *54*, 724–728. [CrossRef]